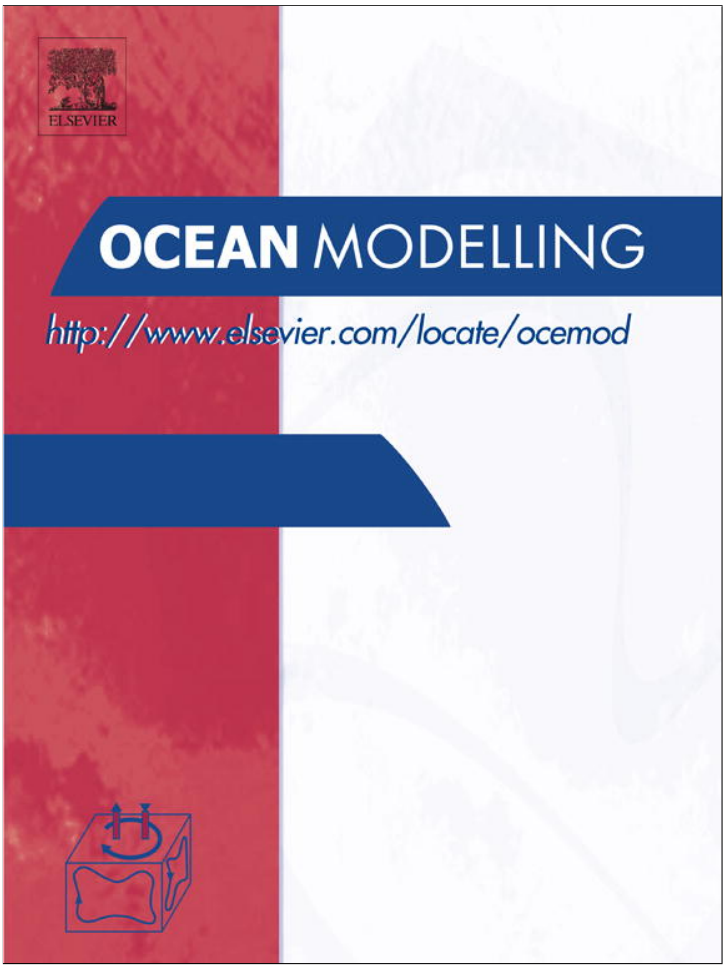

Ocean Modelling 69 (2013) 64–78

Contents lists available at SciVerse ScienceDirect

Ocean Modelling

journal homepage: www.elsevier.com/locate/ocemod

Mitigating horizontal divergence "checker-board" oscillations on unstructured triangular C-grids for nonlinear hydrostatic and nonhydrostatic flows

Phillip J. Wolfram *, Oliver B. Fringer

Environmental Fluid Mechanics Laboratory, Department of Civil and Environmental Engineering, Stanford University, Stanford, CA 94305, USA

ARTICLE INFO

Article history:
Received 7 December 2012
Received in revised form 4 April 2013
Accepted 14 May 2013
Available online 4 June 2013

Keywords:
Unstructured mesh modeling
Triangular C-grid
Implicit (elliptic) and explicit filtering
Horizontal divergence error
Secondary circulation

ABSTRACT

A complication of finite-volume triangular C-grid methods is the numerical emergence of horizontal divergence errors that lead to grid-scale oscillations in vertical velocity. Nonlinear feedback via advection of momentum can lead to numerical instability in velocity modes via positive feedback with spurious vertical velocities induced by horizontal divergence truncation error. Existing strategies to mitigate divergence errors such as direct divergence averaging and increased diffusion do not completely mitigate horizontal vertical velocity oscillations. We present a novel elliptic filtering approach to mitigate this spurious error and more accurately represent vertical velocities via improved calculation of horizontal divergences. These results are applied to laminar curved channel flows, demonstrating the applicability of the method to reproduce secondary flow features.

1. Introduction

Current design of regional coastal ocean models often focuses on resolving unsteadiness under barotropic forcing and frictional losses. These primary balances are well served by an efficient and classic finite volume C-grid approach, which is effectively the lumped RT0 finite element method (Walters et al., 2009). Storage of scalar variables at cell centers with staggered vector quantities normal to cell faces ensures that scalar quantities, such as the barotropic pressure, are tightly coupled to vector quantities such as the horizontal velocity field. The utility of the Cartesian C-grid approach is well known with additional ocean modeling uses such as resolving geostrophic and nonhydrostatic balances [e.g., MITgcm (Adcroft et al., 2004) and ROMS (Shchepetkin and McWilliams, 2005)].

The unstructured triangular C-grid performs well in standard regional coastal ocean modeling contexts [e.g., SUNTANS (Fringer et al., 2006) or UnTRIM (Jankowski, 2009)]. However, applications requiring resolution of Coriolis acceleration or nonlinear momentum advection are often polluted by high-frequency checkerboard error in the cell-centered horizontal divergence. Vertical velocities constructed using horizontal divergences inherit this error, particularly in hydrostatic models. This liability has, to date, precluded use of the triangular C-grids for large-scale ocean modeling (Danilov, 2010; Gassmann, 2011). Hexagonal C-grids, which do not have horizontal divergence noise modes, are an upcoming and promising alternative with recent applications considered by Ringler et al. (2013). However, for triangular C-grid usage, a plausible solution is a filtering operation to prevent this error from amassing in the horizontal divergence. This filtering step is computed explicitly in time and prior to use of the horizontal divergence field in either the nonhydrostatic pressure computation step or continuity equation to obtain the vertical velocity field.

To the authors' knowledge, application of filters to ocean models has been largely restricted to velocity or pressure modes in structured, Cartesian grids. A notable exception is the ICOsahedral Nonhydrostatic (ICON) model family which applies filtering to the divergence by explicitly adding a carefully selected hyper-viscosity term to the equations of motion that compensates for the leading order truncation error term incurred by the discrete horizontal divergence (Rípodas et al., 2009; Wan et al., 2013). Our filtering method to correct horizontal divergence errors for unstructured triangular C-grids with elliptic operators is novel and directly removes grid-scale variability, even for poor quality grids, by construction. We utilize Shapiro digital filters constructed with information local to the point of application of the filter for computational efficiency (Shuman, 1957; Shapiro, 1975). These filter types have been previously applied in structured Cartesian/Curvilinear C-grid ocean models (e.g., in MITgcm (Berntsen et al., 2006) and HYCOM (Klinger et al., 2006)). However, to the authors' knowledge, this is the first application to an unstructured triangular C-grid ocean model.

* Corresponding author. Tel.: +1 720 234 5831.
E-mail address: pwolfram@stanford.edu (P.J. Wolfram).

1463-5003/$ - see front matter © 2013 Elsevier Ltd. All rights reserved.
http://dx.doi.org/10.1016/j.ocemod.2013.05.007

In this paper we present new filtering methods to remove spurious horizontal divergence modes and subsequently improve vertical momentum advection. A review of the manifestation of horizontal divergence noise in unstructured triangular C-grid ocean models is given in Section 2. Explicit and implicit filtering techniques to mitigate noisy horizontal divergence fields are discussed and developed in Section 3. Numerical diffusion and physical effects of the proposed filters are analyzed in Section 4. The applicability of the horizontal divergence noise removal method is demonstrated by numerical experiments using the open-source unstructured C-grid ocean model SUNTANS to simulate secondary circulation in a curved channel flow (Section 5).

2. Causes and effects of horizontal divergence noise

2.1. Previous studies of horizontal divergence noise

Horizontal divergence noise is often characterized by checkerboard patterns in the horizontal divergence. These noise patterns can arise in transient as well as quasi-steady regimes, independently resulting from poor resolution or widely-used, inconsistent computations of barotropic gradients, viscosity, and Coriolis forcing (Le Roux et al., 2007; Danilov, 2010; Gassmann, 2011). The noise may manifest itself irrespective of boundary conditions. Noise levels increase for nonuniform, fully unstructured grids, but are present even for idealized, periodic equilateral grids with varying bathymetry or even uniform bathymetry on the f-plane (Danilov, 2010; Gassmann, 2011). The noise is an intrinsic property of the grid because Fourier and truncation error analysis for the horizontal divergence operator reveal that the first-order term for the horizontal divergence error has an alternating sign between upward and downward pointing triangles (Danilov, 2010; Wan et al., 2013). As detailed in depth by Gassmann (2011), this problem with horizontal divergence noise corresponds to an inability of neighboring triangles sharing an edge to have the same analytical divergence. The problem is unfortunately independent of the divergence discretization, but is limited to the triangular C-grid as it does not occur for the hexagonal C-grid (Gassmann, 2011). The severity of the error incurred will depend on both the discretization used and dynamics. Unfortunately, many implementations and flows of interest manifest this horizontal divergence checkerboarding error which is most readily observable in a checkerboarded vertical velocity (Danilov, 2010; Gassmann, 2011; Wan et al., 2013).

The simplest approaches to mitigate the triangular divergence checker-boarding error are direct averaging, increased diffusion, or hyper-viscosity. However, averaging only veils the noise and cannot prevent its further manifestation via nonlinear feedback (Gassmann, 2011). Damping of the spurious divergence via increased diffusion does not in general mitigate the problem, particularly if boundary layers are unresolved, because common implementations of the diffusion operator are anisotropic in general (Danilov, 2010). Furthermore, as shown by Holleman et al. (2013), diffusive truncation errors related to advection are anisotropic. The combined physical and numerical diffusion, consequently, is in general anisotropic and cannot mitigate the error. Explicit hyper-viscosity approaches, although successful, require tuning of a hyper-viscosity coefficient to ensure the checkerboarding error is mitigated (Wan et al., 2013). A new approach, in development by Peter Korn of MPI Hamburg, utilizes mimetic methods to constrain the horizontal divergence error by application of projectors to and from the primal and dual grids to ensure discrete operators behave analogously to their continuous counterparts (Korn, 2011).

We acknowledge these challenges and propose a new strategy to prevent spurious feedback of this noise within an ocean modeling framework. The divergence noise mode contaminates all fields simultaneously because the discretization and dynamics are coupled. However, the impacts of the noise depend on the discretization and solution methodology. For example, the noise modes may be most identifiable within the horizontal velocity field or horizontal divergence field depending on whether equations are formulated with respect to face velocities or horizontal divergences because these are intrinsically related via the Helmholtz decomposition (Nicolaides, 1992). We therefore examine the current design of ocean models to design a methodology to mitigate horizontal divergence error.

2.2. Horizontal divergence errors in an idealized triangular C-grid ocean model

A generalized ocean model consists of a continuity equation and momentum equation, viz

$$\frac{\partial w}{\partial z} + \nabla_H \cdot \boldsymbol{u}_H = 0 \tag{1}$$

$$\frac{\partial \boldsymbol{u}}{\partial t} = \boldsymbol{F} - g\nabla_H \eta, \tag{2}$$

where the subscript H indicates the horizontal components of a vector, η is the free surface, $\boldsymbol{u}$ is the velocity vector, g is the gravitational constant, t is time, z is the vertical coordinate, and $\boldsymbol{F}$ is a forcing term aggregating advection of momentum, the baroclinic pressure gradient, nonhydrostatic pressure, viscous dissipation, Coriolis, wind stresses, etc. The free surface elevation is obtained via the depth-averaged continuity equation

$$\frac{\partial \eta}{\partial t} + \nabla_H \cdot \int_{-d}^{\eta} \boldsymbol{u}_H dz = 0, \tag{3}$$

where d is the depth.

For a C-grid discretization, a face-normal horizontal momentum equation is obtained by dotting a face-normal vector, $\boldsymbol{n}$, with Eq. (2). It is applied at cell edges j for the face-normal velocity U_j, viz

$$\frac{\partial U_j}{\partial t} = F_j - g\left.\frac{\partial \eta}{\partial n}\right|_j, \tag{4}$$

where $F_j = \boldsymbol{F}\cdot\boldsymbol{n}$ and $g\left.\frac{\partial \eta}{\partial n}\right|_j = \boldsymbol{n}\cdot\nabla_H\eta$. The continuity equation (3) is used to update the free surface in a cell. In the case of the θ-method of Casulli and Zanolli (2002), the momentum and continuity equations are solved simultaneously to yield predicted values for the edge momentum U^* and free surface η^*. For the hydrostatic case these values are simply $U^{n+1} = U^*$ and $\eta^{n+1} = \eta^*$. However, if nonhydrostatic pressure is utilized, w^* is computed via a vertical momentum equation and the nonhydrostatic pressure-correction field qc is calculated with an elliptic equation for the corrector step to obtain U^{n+1} and η^{n+1}(Fringer et al., 2006). For both the hydrostatic and nonhydrostatic methods, continuity is strictly enforced by prognostically computing vertical velocities w^{n+1} via a nonhydrostatic pressure correction imposing a discrete version of Eq. (1),

$$w^{n+\theta}_{i,k+1} = w^{n+\theta}_{i,k} - D_H(U^{n+\theta}\Delta z)_{i,k}. \tag{5}$$

The horizontal divergence of U^{n+1} over each z-level of thickness Δz for horizontal divergence is given by

$$D_H(U^{n+\theta}\Delta z)_{i,k} = \frac{1}{A_i}\sum_{m=1}^{Ns} U^{n+\theta}_{m,k}\Delta z_{m,k} N_m df_m, \tag{6}$$

where it is assumed that $U_{m,k}$ and $\Delta z_{m,k}$ are evaluated at face m and level k, df_m is the length of a face, and A_i is the cell area (Fringer

et al., 2006). Errors in U are consequently projected onto the vertical velocity.

Spurious modes can be suppressed for a single layer if the external Rossby radius is resolved for a barotropic flow, which is typically the case, because the vertical velocity is coupled to the free-surface pressure gradient directly (Danilov, 2010). However, for the general multi-layer case, truncation errors deriving from the calculation of the horizontal velocities are passed into each layer of the vertical velocity field because no explicit additional constraint is placed on the horizontal divergences to constrain the spurious modes. The errors can thus vary in each layer, particularly for a complex flow. The depth-integrated sum of these errors ultimately influences the free surface, but since the error for a cell in a column is generally distinct from the other layers in the column, the free surface does not eliminate the error in each layer. More importantly, the resultant oscillations in vertical velocity subsequently contaminate advection of momentum and scalar transport. These errors will vary based on choice of grid, the flow, and the number of layers. Grid topology, in particular, has a strong influence on resultant spurious modes in the horizontal divergence and vertical velocity field.

2.3. Triangular grid topology

In order to fully illustrate spurious horizontal divergence modes we introduce three general classes of triangular C-grids, as shown in Fig. 1. The distinctions between these grid types is important because they will be used to demonstrate additional complexities encountered in fully unstructured simulations not considered in previous studies of horizontal divergence noise (Danilov, 2010; Gassmann, 2011).

Triangular grids may be structured or unstructured. In a structured equilateral grid there are two types of triangles, each pointing in opposite directions as shown in Fig. 1(a) with upward and downward pointing triangles. Naturally, six cells share a node and all cells are equilateral and the same size. For a fully unstructured grid, this is no longer the case as illustrated in Fig. 1(b), where triangles point in multiple directions and clusters of five, six, or seven cells share a node. Cells are not necessarily equilateral and may change size to better represent boundaries or multiscale physics. For curvilinear and simplified geometries, a hybrid approach may be utilized as shown in Fig. 1(c) in which six cells strictly share a node. Cells are no longer strictly equilateral and may be stretched and rotated to accommodate the system geometry. All grids in Fig. 1 are orthogonal, such that a line between the circumcenters of cells sharing an edge is normal to the edge (Casulli and Zanolli, 2002).

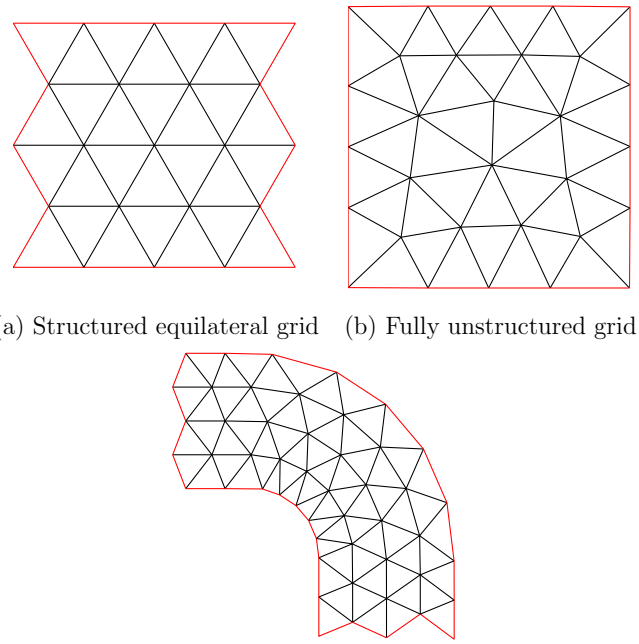

(a) Structured equilateral grid (b) Fully unstructured grid

(c) Hybrid grid

Fig. 1. Types of triangular grids where the fully unstructured grid (b) has vertices shared by five, six, and seven cells. The structured equilateral (a) and hybrid grids (c) have vertices shared by six cells.

2.4. Fundamentals of spurious horizontal divergence modes

Consistent with common practice in ocean modeling we presume that the horizontal velocity field on a particular grid has been previously calculated, with the diagnostic horizontal divergence operator given by Eq. (6). The null space of D_H is always nonempty according to the rank theorem and is spanned by horizontal velocities U which describe all grid-resolvable horizontally divergence-free modes. An analytically divergence-free flow $\boldsymbol{u}$ may have horizontal divergence truncation errors corresponding to discretized velocity components U that are not in the null space of D_H, such that $D_H U = T.E.$ yields the truncation error $T.E.$ Wan et al. (2013) present the analytical truncation error for the horizontal divergence and show its strong dependence upon triangle orientation. A straightforward, physical example of the consequences of the horizontal divergence null space has already been presented by Danilov (2010) for the case of horizontal divergence beneath the surface Ekman layer in a periodic, zonally reentrant flow driven by wind.

The structure of the truncation errors is readily discernible with a simple example. We note that this analysis may exaggerate the impacts of the divergence noise because in general the noise will be problem specific and accentuated for nonlinear flows. However, the analysis qualitatively illustrates the relationship between the noise and solution wavenumber. If we denote the horizontal divergence, which is exact in the limit $A_i \to 0$, as

$$\mathcal{D}_{exact} = (\nabla \cdot \vec{u})_i = \frac{1}{A_i} \int_{A_i} \nabla_H \cdot \boldsymbol{u}_H dA_i$$

and the discrete divergence operator as $\mathcal{D}_i = D_H[\boldsymbol{u}(\boldsymbol{x}_j) \cdot \boldsymbol{n}_j]$ where $\boldsymbol{x}_j$ is the location of the jth edge mid-point, then a normalized measure of the numerical truncation error is given by $E = (\mathcal{D}_{exact} - \mathcal{D}_i)/\max|\mathcal{D}_{exact}|$. This error is computed on structured triangular grids with edge-aligned and edge-normal flows at grid-scale high wavenumber k_G and domain-scale low wavenumber k_D as shown in Fig. 2. For the edge-aligned flows, the velocity field $\boldsymbol{u} = \cos(kx)\hat{i}$ produces a diamond pattern for both low and high wavenumbers in Fig. 2(a) and (c), respectively. For this case, $k_D = 2\pi$ and $k_G = 2\pi/\Delta x$, where Δx is the triangle edge length. The diamond pattern is essentially striping in a direction normal to the flow. This is in direct analogy to Cartesian grids exhibiting repeating stripe pairs along columns or rows. Structured hexagonal grids also exhibit repeating stripe pairs for edge-aligned flows as well as the possibility of repeating stripe triplets for edge-normal flows. In contrast, for a triangular grid, edge-normal flows respond differently and for $\boldsymbol{u} = \cos(ky)\hat{j}$ checker-boarding occurs. For this case, the shortest resolvable scale is smaller than the triangle edge length and is $\sqrt{3}\Delta x/2$, and thus the highest wavenumber $k_G = 4\pi/\left(\sqrt{3}\Delta x\right)$. At this wavenumber, E is a checkerboard pattern over the whole grid as shown in Fig. 2(d). The smallest wavenumber for the edge-normal flow is $k_D = 2\pi/\left(2\sqrt{3}\Delta x\right)$, and in this case the checkerboard is only manifest in localized regions, in this case in the center of the grid as in Fig. 2(b). Owing to directional dependence, the

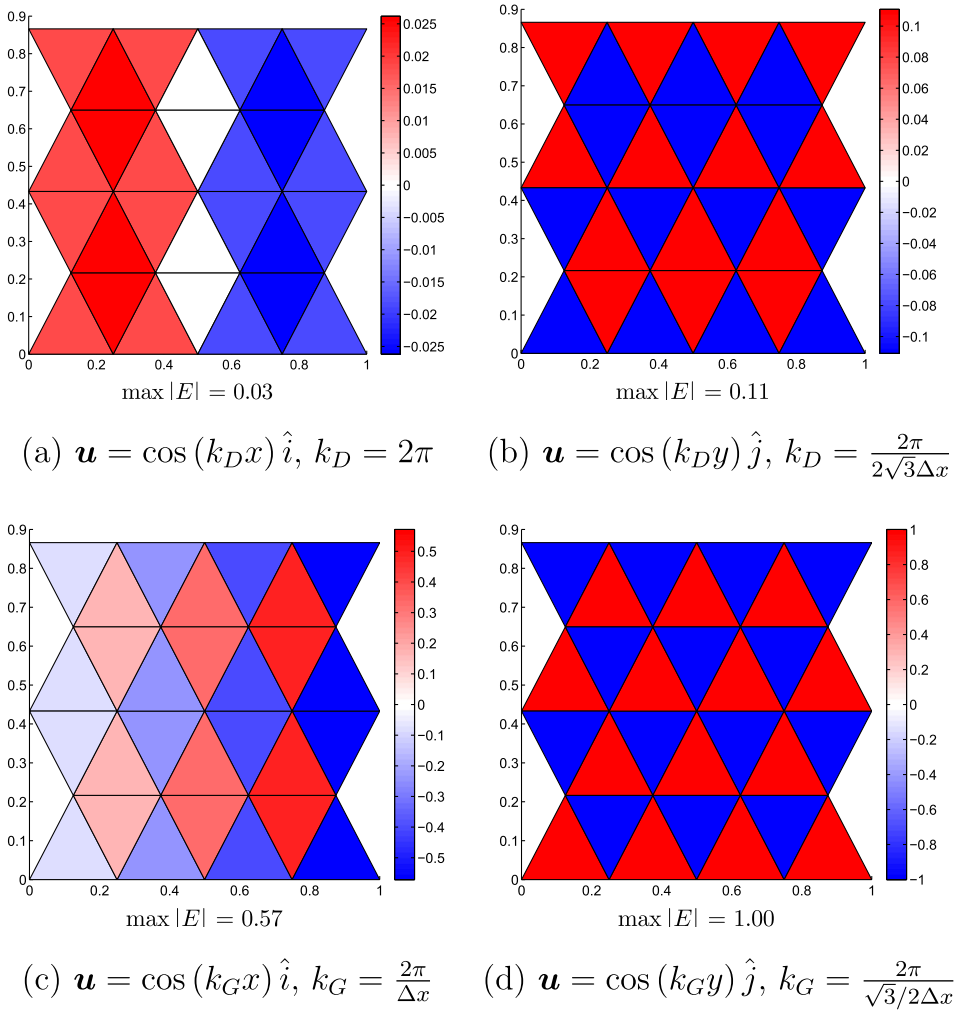

Fig. 2. Normalized horizontal divergence truncation error E for structured grid comparing edge-aligned, $\boldsymbol{u} = \cos(kx)\hat{i}$ (left column), and edge-normal, $\boldsymbol{u} = \cos(ky)\hat{j}$ (right column), flows for low wavenumbers corresponding to the domain length scale, k_D (top row), and high wavenumbers corresponding to the grid-scale, k_G (bottom row). Distinct error patterns such as striping (left column) or checker-boarding (right column) emerge for these orthogonal cases.

truncation error for a solid-body rotational vortex will vary corresponding to the orientation of the flow, thereby inducing spurious vertical flows. Errors are greatest for high wavenumbers, although ultimately nonlinear processes and geometrical inhomogeneities produce solution degradation.

The magnitude of horizontal divergence errors is less variable with respect to flow directions for the unstructured grid as compared with the structured grid, as shown in Fig. 3. In particular, the checker-board pattern is less distinct but more prevalent with respect to the flow direction. A constraint is required to address these errors, particularly since they vary with rotation of the velocity vector as shown in Fig. 3(a) corresponding to a zonal flow and Fig. 3(b) corresponding to a meridional flow. Free surface gradients are insufficient because horizontal divergence errors will not be constant over depth for a complex flow.

A fully 3D flow will vary over depth, resulting in vertically variable error. Consequently, horizontal divergence error cannot in general be damped by a depth-averaged constraint. Without application of a unique constraint in each layer, small spurious checker-board structured horizontal divergence noises can grow via nonlinearity to dominate the momentum balance and mask the correct velocity signal. Thus, the horizontal divergence error must be mitigated separately in each layer via a direct application of a spatial filter at each time step.

3. Horizontal divergence noise removal

3.1. Explicit filters

Explicit filtering, as described by Gassmann (2011), effectively redefines the horizontal divergence as an averaged horizontal divergence operator, $D_{H,F}$ of the form $D_{H,F}U = F_c D_H U$, where F_c represents a filtering, or averaging operation, on cell values. Alternatively, it is possible to explicitly filter U such that $D_H F_e U \approx F_{c,eq} D_H U$ for an edge filter F_e in hopes that the resultant $F_{c,eq}$ adequately smooths the divergence field. For the F_c filter, cell horizontal divergence values are averaged to cell edges or nodes and then interpolated back onto the cell via a diffusional smoothing process with diffusion coefficient $\nu_F \sim \mathcal{C}\Delta x^2/\Delta t$ (Shuman, 1957; Shapiro, 1975), where Δx is a measure of the triangular spacing, Δt is the time step size, and $\mathcal{C}$ is a constant. The F_e filter averages velocity values to cells and then back onto edges.

The explicit method for directly filtering the horizontal divergence has several inherent problems. Horizontal divergence errors inherently remain in $D_H U$ and can potentially be amplified over the course of several time steps. Thus, the error can still pollute the solution via nonlinear feedback as noted by Gassmann (2011). Secondly, continuity is not strictly enforced in each cell since the discrete diagnostic equation for the vertical face-velocity in each cell $w_{i,k}$ becomes

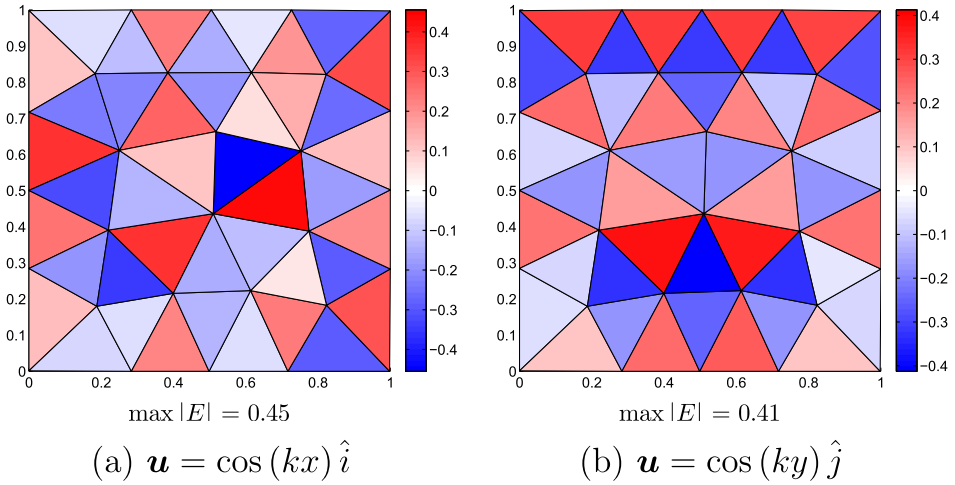

Fig. 3. Normalized horizontal divergence truncation error E for (a) $\boldsymbol{u} = \cos(kx)\hat{i}$ and (b) $\boldsymbol{u} = \cos(ky)\hat{j}$ for high wavenumber $k = \frac{2\pi}{\Delta x_{max}}$ with $\Delta x_{max} = 0.31$ showing variability of E with respect to rotation of a constant velocity field. Low domain-scale wavenumber maximum error (not shown) corresponding to $k = 2\pi$ is $\max|E| = 0.1$.

$$w^{n+\theta}_{i,k+1} = w^{n+\theta}_{i,k} + F_c D_H (U^{n+\theta}\Delta z)_{i,k},$$

not the precise Eq. (5) as derived from continuity equation (1). Direct application of the filter to the horizontal divergence field violates continuity by effectively adding a diffusion term to the continuity equation.

A seemingly better alternative is explicit filtering of U via $F_e U$ in hopes that $D_H F_e U$ is smooth. This ensures that continuity is satisfied, although it may not necessarily ensure that the horizontal divergence field is smooth. Furthermore, the effective redefinition of the horizontal divergence operator by $D_H F_e$ removes the skew symmetry relationship between the gradient and divergence operators, i.e., $D_H F_e \neq -G^T$. The applicability of this method will be considered further when filtering operators are defined.

3.2. Implicit filters

Implicit filtering removes horizontal divergence noise by elliptically correcting U such that the resultant horizontal divergence field is smooth, i.e., using

$$D_H U_F = F_c D_H U \tag{7}$$

to compute a filtered horizontal velocity field U_F. This removes the oscillatory horizontal divergence noise from the velocity field thereby preventing its propagation and preserving discrete continuity.

Implicit filtering thus requires solution of Eq. (7) to compute a filtered horizontal velocity field U_F. The solution steps are analogous to computation of the nonhydrostatic pressure and take advantage of the discrete Helmholtz decomposition such that the correction step modifies the flow divergence without changing flow vorticity (Nicolaides, 1992):

1. Define a correction using the gradient of a scalar field ϕ,

$$U_F = U - G\phi. \tag{8}$$

2. Form a Poisson equation by taking the horizontal divergence of Eq. (8) and using Eq. (7) as a constraint,

$$D_H U - D_H G\phi = F_c D_H U,$$

$$L\phi = (I - F_c) D_H U, \tag{9}$$

where $L = D_H G$ is the discrete Laplacian and I is the identity matrix.
3. Solve the Poisson equation (9) and compute U_F from Eq. (8).

Unlike computation of the nonhydrostatic pressure field, the source term $(I - F_c)D_H U$ is composed of high wavenumber modes since the filter F_c removes high frequency noise from the horizontal divergence field. As a result, only a few simple and fast Gauss–Seidel iterations, specifically four in practice, are used to solve Eq. (9) quickly. Quick convergence occurs because the iterative method damps the high frequency error from the solution efficiently via application of compact local stencils for L. This is in contrast to the nonhydrostatic pressure computation, which requires a more involved solution method such as the conjugate gradient method to efficiently compute both the low and high wavenumber components of the solution.

3.3. Higher-order filters

A primary physical consequence of implicit filtering is that the horizontal velocity field is also filtered in addition to the horizontal divergence field. This may lead to damping, particularly with first-order filters, which is detrimental to a simulation because it effectively reduces the flow Reynolds number due to the addition of numerical diffusion. Alternatively, a high-order filter may yield spurious oscillations. Design of higher-order hyper-viscous filters is warranted to both prevent and evaluate the damping incurred by low-order filtering.

Several orders of filters can be defined starting with first-order filtering. First-order filtering consists of one filter pass and effectively area-weights velocity or horizontal divergence values at edges or cells to intermediate points during a downsampling step. These values are then interpolated back onto the computational cells and edges during an upsampling step. The primary difference between filter types is the choice of the downsampling step. Edge filters average the values of cells sharing an edge and nodal filters average the values of cells sharing a node to complete the downsampling step.

Development of a second-order filter from the first-order filter occurs recursively once a first-order filter has been defined (Shuman, 1957; Shapiro, 1975). We use prime notation, (e.g., $\phi'' = \nabla^2\phi$), and define

$$F_0\phi = \phi + \nu_G \phi'', \tag{10}$$

as a primitive model for the filtering operation where $\nu_G = \mathcal{C}\Delta x^2/\Delta t$ for some constant $\mathcal{C}$. A single first-order filter pass performs an averaging downsampling step followed by an interpolatory upsampling step. Note that by definition, the first-order filter F_1 is equiv-

alent to a single filter pass, viz $F_1 = F_0^1$. We can construct a higher-order filter F_2 by considering two operations of the first-order filter giving

$$F_0^2\phi = F_0\phi + v_G F_0(\phi'') = \phi + v_G\phi'' + v_G(\phi'' + v_G\phi^{iv}) = \phi + 2v_G\phi'' + v_G^2\phi^{iv}.$$

This can be combined with Eq. (10) to show the desired result of applying hyper-viscosity via the second-order filtering operator,

$$(2F_0 - F_0^2)\phi = \phi - v_G^2\phi^{iv}.$$

It is then a simple matter to perform higher-order filtering via the operator $F_2 = 2F_0 - F_0^2$. An n-order filter F_n is generalized as

$$F_n = \sum_{k=1}^{n}\binom{n}{k}(-1)^{k+1}F_0^k. \tag{11}$$

The key result is that for simple first-order filters F_1 the primary numerical effect is addition of numerical diffusion whereas for the second-order filter F_2 it is hyper-viscosity. This allows greater control to prevent artificial Reynolds number reduction and is a key advantage of the second-order filter. We now define the first-order filters ($F_1 = F_0^1$) necessary to implement these higher-order filters.

3.4. Filter operators

A generalized filter relies upon simple digital Shapiro filter primitive operations which are applied via downsampling (averaging) and upsampling (interpolation) to and from edges or nodes. For purposes of notation, we follow Casulli and Zanolli (2005) and consider an edge j, for cell i, such that $1 \leqslant i \leqslant N_c$, where N_c is the number of cells. The edge is identified by an index connecting cells to edges, viz. $j(i,l)$ such that $1 \leqslant j \leqslant N_e$, where N_e is the number of edges, and $1 \leqslant l \leqslant S_i$ for $S_i = 3$ sides of a triangle. Cells neighboring an edge are specified by an index denoting the cell neighbors to an edge, viz $i(j,\alpha)$ such that $1 \leqslant \alpha \leqslant 2$ denotes both cell neighbors to the edge. Cells sharing an edge are $i(j,1)$ and $i(j,2)$. Necessarily, $1 \leqslant i(j,\alpha) \leqslant N_c$. Nodes are identified by an index connecting cells to nodes, viz $p(i,l)$ such that $1 \leqslant p(i,l) \leqslant N_p$. Cell neighbors sharing nodes are identified by $i(p,\beta)$, such that $\beta = 1,\ldots,N_{pc}$, where N_{pc} is the number of cells neighboring a node, typically ranging between 5 and 7, where 6 is optimal providing the best tessellation of space with triangles. Necessarily, $1 \leqslant i(p,\beta) \leqslant N_c$ and $i(p,\beta_i)$ and $i(p,\beta_j)$ are cells sharing a node for $\beta_i \neq \beta_j$.

An area-weighted representation of averaging a cell-centered scalar to an edge, $\overline{\phi_j}$, and node, $\overline{\phi_p}$, is then

$$\overline{\phi_j} = \frac{\sum_{\alpha=1}^{2}(\phi_i A_i)|_{i(j,\alpha)}}{\sum_{\alpha=1}^{2}A_i|_{i(j,\alpha)}} \tag{12}$$

and

$$\overline{\phi_p} = \frac{\sum_{\beta=1}^{N_{pc}}(\phi_i A_i)|_{i(p,\beta)}}{\sum_{\beta=1}^{N_{pc}}A_i|_{i(p,\beta)}}. \tag{13}$$

Smoothed values are interpolated back onto cell centers via well-known Barycentric interpolation (Wang et al., 2011; Huebner, 1975). This is illustrated in Fig. 4 and given by

$$\phi(\boldsymbol{x}) = \lambda_1\phi_1 + \lambda_2\phi_2 + \lambda_3\phi_3, \tag{14}$$

where each weighting coefficient is the proportional area of the sub-triangle opposite to the node, e.g., $\lambda_1 = A_1/(A_1 + A_2 + A_3)$.

The stencils for some filter methods used in this paper are illustrated in Fig. 5. For brevity, we describe the first-order filters depicted in Fig. 5(a), (c), and (e) below. Extension to the higher-order filters depicted in Fig. 5(b), (d), and (f) is obtained through

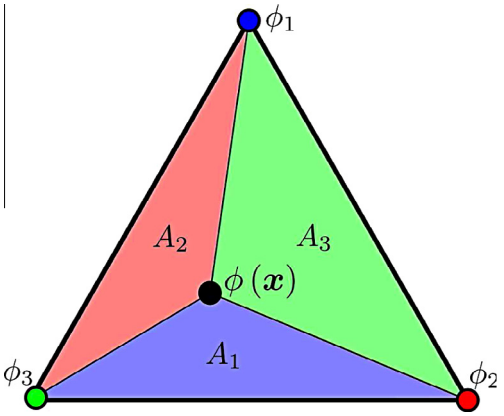

Fig. 4. Barycentric interpolation of scalar ϕ at $\boldsymbol{x}$ from nodal values ϕ_1, ϕ_2, and ϕ_3.

application of Eq. (11) where EP2 denotes a Shapiro second-order explicit Perot filter, IE2 a Shapiro second-order implicit edge filter, IN2 a Shapiro second-order implicit nodal filter, etc. Each filter can be described in terms of a downsampling and an upsampling step, as follows:

1. (EP1) First-order explicit Perot filter
   (a) Downsample face-normal velocities U onto cell centers $\boldsymbol{u}_i$ with the Perot cell-center velocity reconstruction (Perot, 2000),

$$\boldsymbol{u}_i = \frac{1}{A_i}\sum_{m=1}^{N_s}U_m\boldsymbol{n}_m d_{i,m}df_m. \tag{15}$$

   (b) Upsample $\boldsymbol{u}_i$ to edges using Eq. (12) and project via the face normal to obtain F_1U.
2. (IE1) Shapiro first-order implicit edge filter using edge downsampling and upsampling
   (a) Downsample horizontal divergence D_HU to edges with Eq. (12) to obtain $\overline{D_HU}$.
   (b) Upsample $\overline{D_HU}$ from edges to cells with Eq. (14), using triangles formed from edge mid-points, to obtain $F_1(D_HU)$.
3. (IN1) Shapiro first-order implicit nodal filter using node downsampling and upsampling
   (a) Downsample horizontal divergence D_HU to nodes with Eq. (13) to obtain $\overline{D_HU}$.
   (b) Upsample $\overline{D_HU}$ from nodes to cells with Eq. (14), using triangles formed from cell nodes, to obtain $F_1(D_HU)$.

Shapiro (1975) showed that after successive higher-order filtering, damping of low-wavenumber Fourier components was decreased. A filter of sufficient order could, in principle, remove spurious two-delta-x oscillations with very minimal low wavenumber damping.

3.5. Filter implementation

Filter implementation is important because it will modify mass and energy balances. In particular, implicit filtering is required in a hydrostatic code precisely to ensure that the divergence-free constraint in each cell is met. Direct filtering of the vertical velocity without modification of the horizontal velocity would violate continuity in general. Consequently U must be filtered either explicitly or implicitly if w is filtered. Below we outline the non-hydrostatic free surface algorithm with an implicit filtering method that ensures constraint (5) is satisfied for solution of Eqs. (3) and (4):

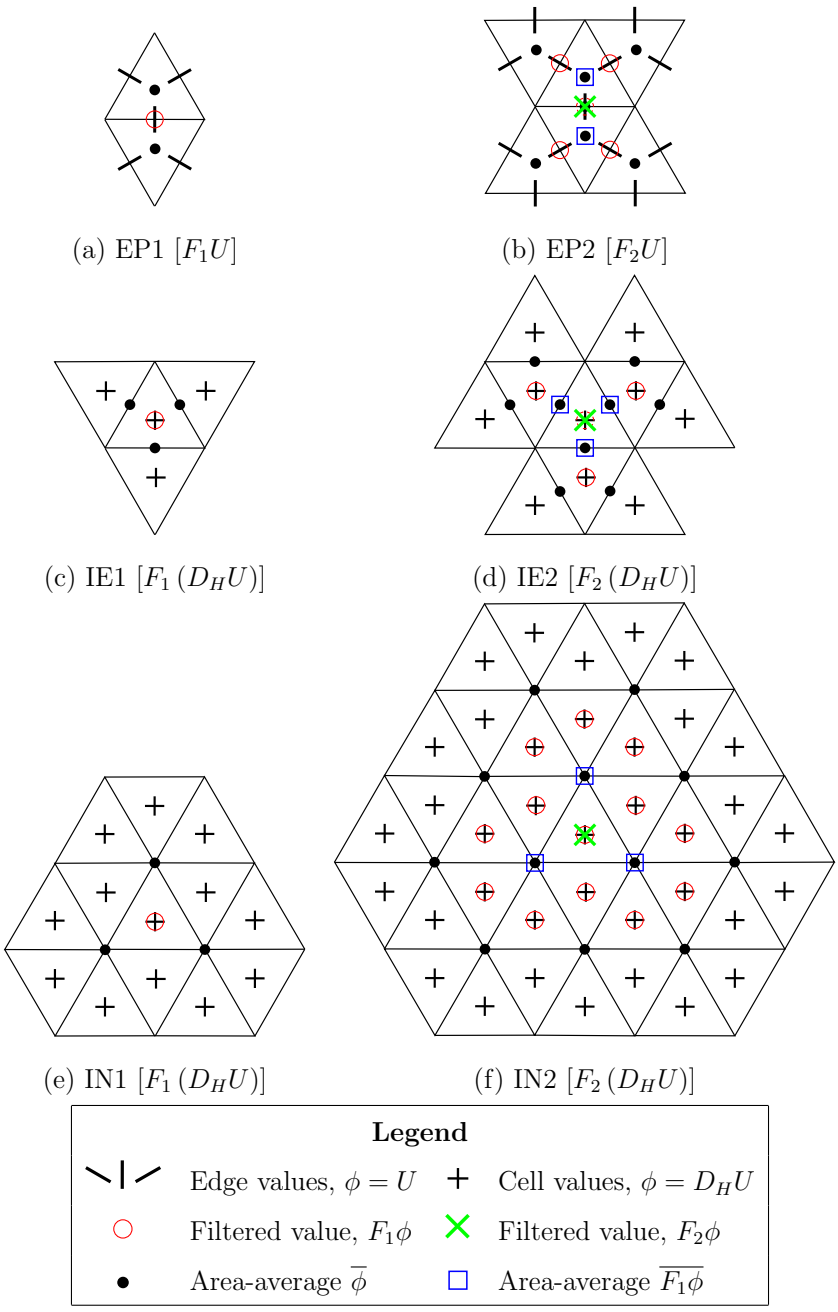

Fig. 5. Filter stencils for scalar value ϕ, where $\phi = U$ for the explicit filters (EP1, EP2) and $\phi = D_H U$ for the implicit filters (IE1, IE2, IN1, IN2).

1. Compute the free surface η^* via the θ-method of Casulli and Zanolli (2002), such that Eqs. (3) and (4) and are solved implicitly.
2. Compute a provisional velocity U^* from Eq. (4). Let $U^k = U^*$ and $\eta^k = \eta^*$ be the start of an iterative method.
3. Implicitly filter the horizontal divergence field at each k level to obtain U_F^k from U^k as in Equations (8) and (9).
4. Correct the filtered field with the nonhydrostatic pressure, qc, if desired. First, compute $w^k = w^*$, the predicted vertical velocity obtained from the vertical momentum balance. Then correct the velocity with

$$U^{k+1} = U_F^k - \Delta t \frac{\partial qc}{\partial x},$$

$$w^{k+1} = w^k - \Delta t \frac{\partial qc}{\partial z},$$

and solve the Poisson equation for qc obtained by imposing constraint (5). Full details are provided in Fringer et al. (2006). For hydrostatic flows, set $U^{k+1} = U_F^k$ and update w^{k+1} via Eq. (5).
5. Update the free surface η^{k+1} using U^{k+1} via the θ-method discretized equation (3).
6. Iterate from step 2 until convergence is obtained. Once converged, set $\eta^{n+1} = \eta^{k_{end}+1}$, $U^{n+1} = U^{k_{end}+1}$, and $w^{n+1} = w^{k_{end}+1}$.

Convergence of the nonhydrostatic iterative procedure was recently shown by Vitousek and Fringer (2012).

Continuity equation (3) is ultimately sacrificed if the free surface is not updated following computation of the filtered velocity U_F^* in step 5. However, because the updated η^{k+1} is not consistent with momentum in Eq. (3), iteration is required. In practice, however, these iterations may be unnecessary to attain reasonable accuracy, as is the case with the example presented in this paper.

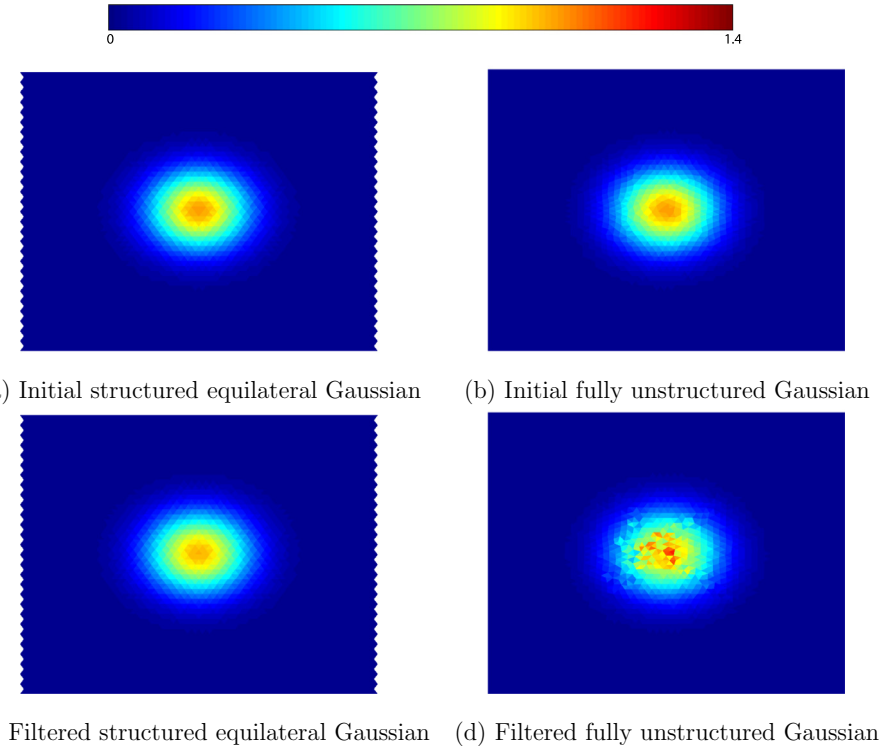

(a) Initial structured equilateral Gaussian (b) Initial fully unstructured Gaussian

(c) Filtered structured equilateral Gaussian (d) Filtered fully unstructured Gaussian

Fig. 6. Demonstration of explicit Perot filtering for normalized, initially Gaussian horizontal divergence fields on (a) structured equilateral and (b) fully unstructured grids. The filtered structured equilateral grid (c) is smooth but the filtered fully unstructured gird (d) is not smooth. The EP1 filter was applied 10 times.

Table 1
Effective nondimensional diffusion coefficient values $K_{max}\frac{\Delta t}{\Delta x^2}$ resulting from horizontal divergence filtering and horizontal velocity filtering on structured equilateral and fully unstructured grids.

Filter	Horizontal divergence		Horizontal velocity	
	Structured	Unstructured	Structured	Unstructured
IE1	0.04	0.07	0.01	0.2
IN1	0.2	0.5	0.04	0.8
IE2	3×10^{-8}	7×10^{-4}	2×10^{-5}	7×10^{-4}
IN2	4×10^{-7}	5×10^{-3}	3×10^{-4}	0.003

Filtering, although necessary to remove the spurious horizontal divergence noise, ultimately affects the problem dynamics. Volume conservation is maintained by construction but energy is not necessarily conserved because implicit filtering removes energy by smoothing the velocity field. In what follows, a modified partial differential equation analysis is used to demonstrate grid-scale dependent spurious physics that results from the filter application.

4. Filter analysis

4.1. Physical effects of explicit and implicit filters

We return to our first-order filter model $F\phi = \phi + v_G\phi''$ and consider the effect of filtering on the horizontal divergence field and the horizontal velocity field. Although in reality grid inhomogeneity will produce ansiotropic diffusion, here we analyze the simple case of isotropic diffusion on structured equilateral grids. We first consider the case D_HF_eU for the Perot edge filter EP1. Utilizing our model, we obtain

$$F_eU \approx [\boldsymbol{u}_H + v_G\nabla_H^2\boldsymbol{u}_H]\cdot\boldsymbol{n},$$

where the filter adds grid-scale diffusion v_G to the velocity field. The effect is to also add grid-scale diffusion to the horizontal divergence field, since

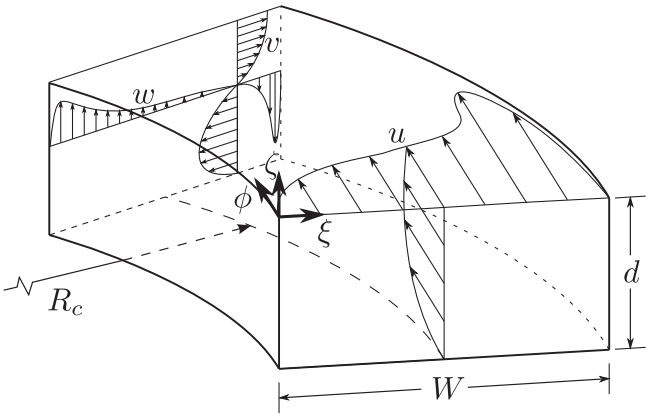

Fig. 7. Axisymmetric curved channel flow where ϕ is the streamwise coordinate, ξ is the transverse direction, and ζ is the vertical direction. The primary flow is composed of a streamwise velocity u and the secondary flow is composed of the transverse and vertical velocity v and w, respectively. The channel is completely defined by its radius of curvature to the channel centerline, R_c, the channel width, W, and the depth, d.

$$D_HF_eU \approx \nabla_H\cdot\boldsymbol{u}_H + v_G\nabla_H^2(\nabla_H\cdot\boldsymbol{u}_H), \tag{16}$$

where we have assumed $\nabla_H v_G = 0$.

The implicit filter $D_HU_F = F_cD_HU$, as utilized for the edge and node cases IE1 and IN1, results in

$$F_cD_HU \approx \nabla_H\cdot\boldsymbol{u}_H + v_G\nabla_H^2(\nabla_H\cdot\boldsymbol{u}_H), \tag{17}$$

with grid-scale diffusion added to the horizontal divergence field. The implicit elliptic correction step yields

$$U_F \approx [\boldsymbol{u}_H + v_G\nabla_H(\nabla_H\cdot\boldsymbol{u}_H)]\cdot\boldsymbol{n},$$

where application of the vector identity $\nabla(\nabla\cdot\boldsymbol{A}) = \nabla^2\boldsymbol{A} + \nabla\times(\nabla\times\boldsymbol{A})$ produces

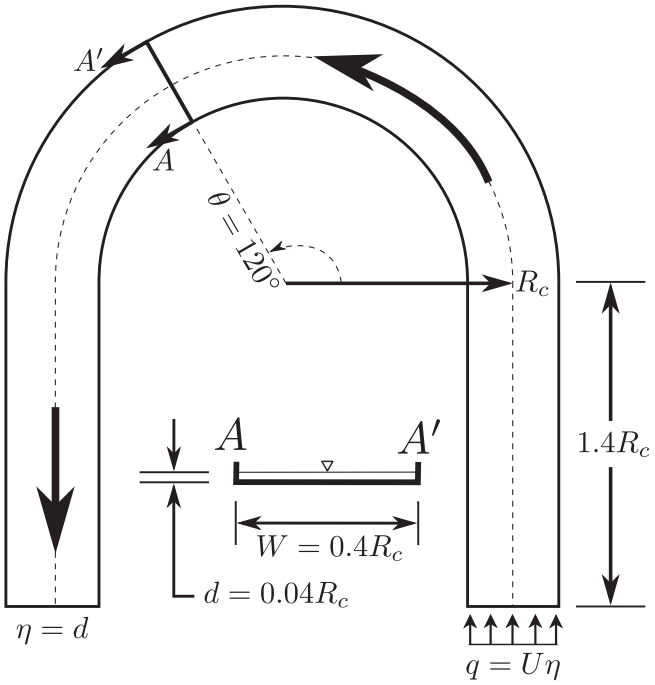

Fig. 8. Simulation geometry for curved channel flow in a 180° bend. Flow is in the counter-clockwise direction. Profiles for comparison with the deVriend, 1981a analytical solution are taken at section A–A'.

$$U_F \approx [\boldsymbol{u}_H + \nu_G \nabla_H^2 \boldsymbol{u}_H + \nu_G \nabla_H \times (\omega_k \boldsymbol{k})] \cdot \boldsymbol{n}, \tag{18}$$

where $\omega_k = (\nabla_H \times \boldsymbol{u}_H) \cdot \boldsymbol{k}$, and $\boldsymbol{k}$ is the vertical unit vector. The common grid-scale diffusion term is obtained, consistent with the horizontal divergence. Ultimately, this term results in energy dissipation. The additional horizontal curl of vertical vorticity term has no standard analog in the governing equations and is consequently completely spurious. The physical viscosity ν must be much larger than grid-scale dependent viscosity ν_G to ensure a physical solution because the effects of the vorticity term may be pronounced and result in spurious oscillation as shown by the third-order filter cases for the highly nonlinear curved channel flow.

4.2. Numerical diffusion induced by filtering

A practical estimate of filter performance can be determined by computing effective numerical diffusion coefficients K via the method of moments (Aris, 1956), a technique recently used by Holleman et al. (2013). We utilize a non-dimensional domain containing a normalized Gaussian horizontal divergence distribution with $\sigma_x = \sigma_y = 10\Delta x$. The Gaussian divergence field is repeatedly filtered to estimate the average spread in divergence corresponding to each application of the filter.

The equivalent horizontal diffusion applied by the filters is calculated for the structured equilateral and fully unstructured cases, which provide bounds on the estimated diffusion coefficient. Diffusion coefficients are also estimated for the second-order filters to quantify their change to the divergence and velocity distributions, although their primary physical effect is hyper-viscosity.

As shown in Fig. 6, the Perot filter EP1 fails to ensure a smooth horizontal divergence field for a fully unstructured grid because it artificially increases the magnitude of the horizontal divergence field. This effect is exemplified by the differences between panels 6(b) and (d). Consequently, the EP1 method, in general, fails to ensure that the noise in the horizontal divergence field is reduced. In fact, the case presented in Fig. 6 actually increases the noise. This issue prevents its further consideration as a viable horizontal divergence error mitigation technique. The implicit edge and nodal filters, in contrast, ensure a smooth horizontal divergence field by construction.

Effective nondimensional diffusion coefficients for the implicit horizontal divergence filters are given in Table 1 for the structured equilateral and fully unstructured grids used in Fig. 6. K_{max} is the maximum of the principal values of the diffusion tensor and provides an upper bound estimate on the diffusion of the method as applied to an unstructured grid. The effective nondimensional diffusion is also presented for the horizontal velocity field based on use of a Gaussian horizontal velocity field oriented in the $\hat{i}+\hat{j}$ direction. Unstructured grid inhomogeneity leads to larger error because cross terms become important, as noted by Holleman et al. (2013). The cross terms give rise to a larger effective diffusion coefficient as estimated from the maximum principal eigenvalue of the diffusion tensor. The added diffusion for the unstructured grids are often an order of magnitude or more greater than that for structured grids.

The overall best method based on this analysis is the second-order edge filter IE2 because the edge filter is less diffusive than the nodal filter. However, the topology of the grid will influence filter choice in practice. For example, the Perot methods EP1 and EP2 have similar diffusivity as the edge methods IE1 and IE2, respectively. However, explicit filter methods EP1 and EP2 fail to ensure a smooth divergence field for an unstructured grid and explicit filtering with these methods is not suitable.

A promising explicit filter alternative currently in development is Peter Korn's mimetic discretization (Korn, 2011) of the ICON model (Rípodas et al., 2009), which applies projectors to each term of the constitutive equations in accordance with consideration of the spaces they occupy. In particular, the lumped mass-matrix implementation of this mimetic method is easily invertible and may provide the theoretical basis for development of an explicit filter family devoid of the drawbacks of the present EP1 and EP2 filters.

Use of hyper-viscosity based second-order filters IE2 and IN2 is currently the most viable filtering option. These filters have less impact on reducing the effective Reynolds number because their continuous equivalent does not have a diffusion term. However, the nodal filter IN2 is more robust than the edge filter IE2 because it downsamples over a wider stencil to a smaller number of values, consequently minimizing the effects of grid topology.

5. Secondary circulation in curved channels

5.1. Test case introduction

Flow in curved channels is similar to Ekman flows with an effective Coriolis acceleration of $f \sim U/R$, where U is the streamwise flow along a bend with radius of curvature R. Thus, because the effective Coriolis term is nonlinear, instabilities related to momentum advection will be amplified in contrast to the classic linear Ekman flow. The effect for the curved channel case is to accentuate horizontal divergence noise because of its sensitivity to the vertical velocity. Furthermore, the analytical solution of the classic laminar axisymetric curved channel with secondary circulation is well known (deVriend, 1981a,b). Because of low aspect ratios (i.e., depth/horizontal scale) ocean flows are typically hydrostatic and nonhydrostatic pressure correction is inadequate to eliminate horizontal divergence noise. Taking this into consideration, we use a curved channel geometry with a low aspect ratio that is very weakly nonlinear such that the filtered hydrostatic flow compares well with the analytical nonhydrostatic solution. The hope is that

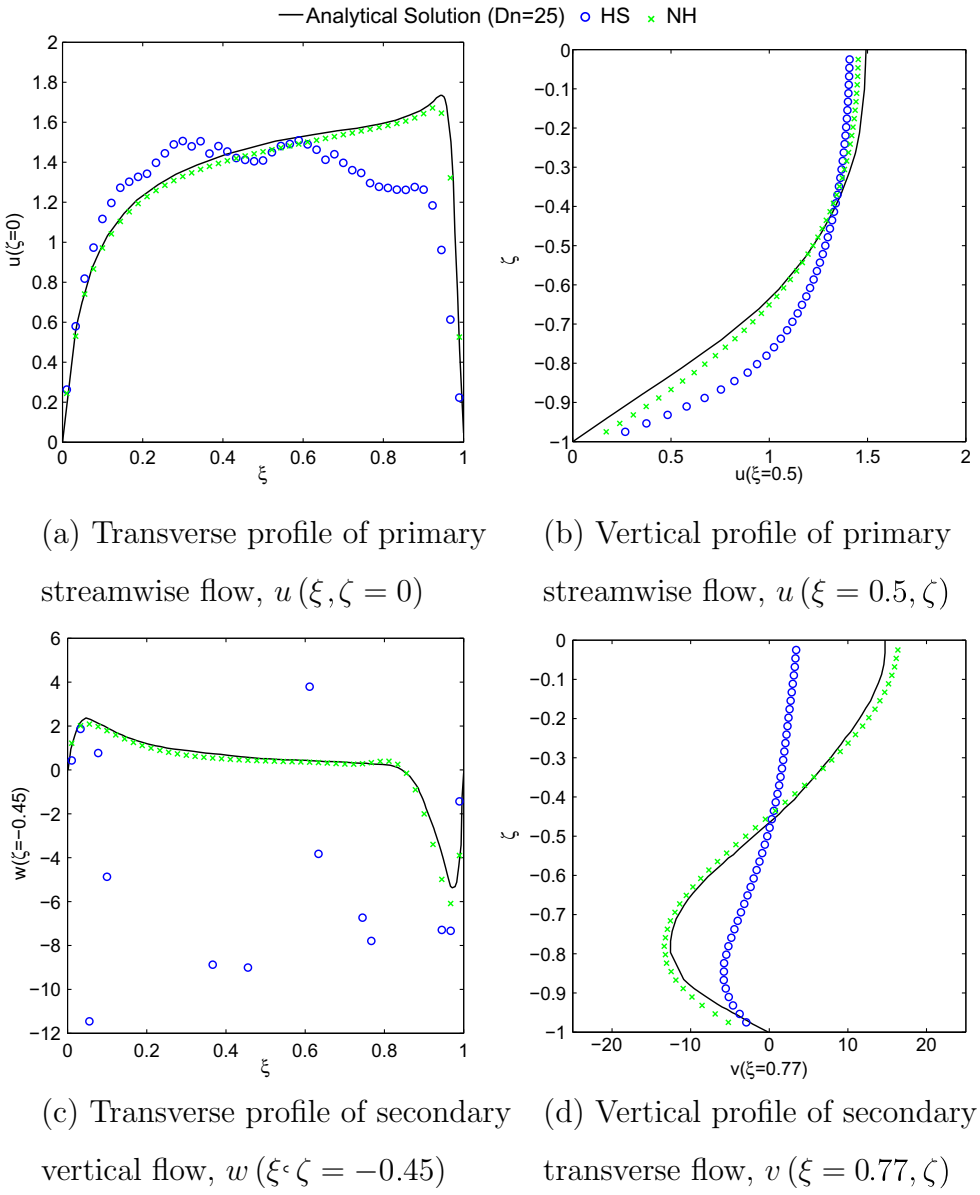

(a) Transverse profile of primary streamwise flow, $u\,(\xi, \zeta = 0)$

(b) Vertical profile of primary streamwise flow, $u\,(\xi = 0.5, \zeta)$

(c) Transverse profile of secondary vertical flow, $w\,(\xi, \zeta = -0.45)$

(d) Vertical profile of secondary transverse flow, $v\,(\xi = 0.77, \zeta)$

Fig. 9. Comparison of non-filtered nonhydrostatic (NH – green ×) and hydrostatic (HS – blue ○) cases on grid FHY. Velocity profiles are plotted transverse to the flow along transect *A*–*A*′ and are compared to the analytical results of deVriend (1981a). Reasonable agreement is obtained between NH and the analytical solution for $Dn = 25$. (For interpretation of the references to color in this figure legend, the reader is referred to the web version of this article.)

the results for filtering hydrostatic flows will be useful for other hydrostatic oceanic flows because computation of the nonhydrostatic pressure correction is impractical in large-scale ocean modeling.

The curved channel geometry, primary flows, and secondary flows are shown in Fig. 7. The nondimensional streamwise coordinate and velocity are ϕ and u, respectively. Secondary circulations are composed of the transverse and vertical velocities v and w corresponding to the ξ and ζ directions, respectively. We do not repeat the governing equations of deVriend (1981a,b) for brevity, but note that the primary flow u is driven by a pressure-viscous balance. The secondary flows v and w are forced by an Ekman-type balance in which an effective Coriolis force balances friction on the channel bottom. The effective nonlinear Coriolis acceleration (ur^{-1}) applies for cylindrical advection of momentum via terms $(ur^{-1})v$ and $(ur^{-1})u$ for the equations of streamwise velocity u and transverse velocity v, respectively. Here, r is the radial distance from the center of curvature.

The problem physics can be described in terms of four nondimensional numbers composed of the variables W, d, R_c, U, ν, and g (See Fig. 7). The rigid lid assumption is utilized owing to the condition in which the Froude number $Fr = U/\sqrt{gd} \ll 1$. As such, the problem is uniquely prescribed in terms of the aspect ratio $\delta = d/W$, Reynolds number $Re = Ud/\nu$, and Deans number $Dn = Re\sqrt{\varepsilon}$ with curvature aspect ratio $\varepsilon = d/R_c$.

We use a modified version of the open-source SUNTANS coastal ocean model [1] (Fringer et al., 2006) and consider weakly nonhydrostatic flows with $Fr \ll 1$, $\delta = 0.1$, $\varepsilon = 0.04$, and $Dn = 25$ corresponding to $Re = 125$ for comparison with the analytical solutions provided by deVriend (1981a,b). In order to compute a flow that is as axisymmetric as possible to match the solution of deVriend (1981a,b), we utilize a 180° bend. Boundary conditions are a prescribed inflow velocity and zero-pressure at the outflow with

[1] Available at http://www.sourceforge.net/projects/suntans/.

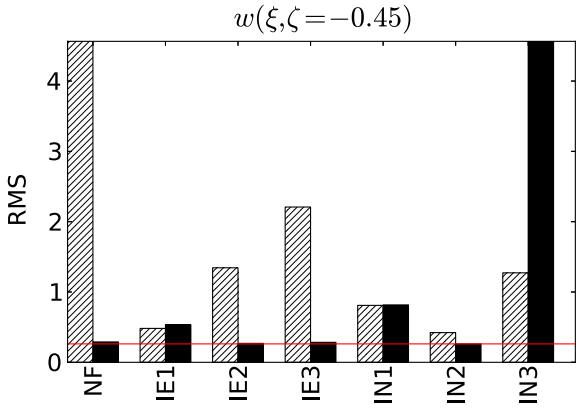

Fig. 10. RMS error for filtered and unfiltered hydrostatic (cross-hatched bars) and nonhydrostatic flow (solid black bars) transverse profile of secondary vertical flow, $w(\xi,\zeta=-0.45)$ (see Fig. 9). The red line denotes minimum RMS error. Entry abbreviations used: NF is no filter, IE1 is first-order implicit edge, IE2 is second-order implicit edge, IE3 is third-order implicit edge, IN1 is first-order implicit node, IN2 is second-order implicit node, IN3 is third-order implicit node. (For interpretation of the references to color in this figure legend, the reader is referred to the web version of this article.)

sufficiently long inlets and outlets to allow for developed flows at the inlet and outlet to the curved channel as shown in Fig. 8. All quantities hereafter are in nondimensional units (star notation is omitted for clarity) following the nondimensionalization presented by deVriend (1981a). Central-differencing momentum advection is utilized with cell-centered velocities obtained with Eq. (15) and advanced with third-order accurate explicit Adams–Bashforth time stepping over 23 flow-through periods from rest with Courant numbers $\mathcal{O}(0.1)$. The model is only strictly first-order accurate in space and very fine resolution is needed to resolve viscous wall layers.

Several test cases are used to examine the performance of filters with respect to hydrostatic and nonhydrostatic flows on different grids with parameters listed in Appendix A, Table A.1. Orthogonal unstructured grids were generated with the TOM grid generator (Holleman et al., 2013). The accuracy of filtered model results are assessed with a fine hybrid grid, denoted by FHY. Next, coarser hybrid and uniform resolution fully unstructured grids (denoted by CHY and CUN) are utilized to qualitatively demonstrate hydrostatic filter impacts on vertical velocity smoothness. Filter performance is then compared for grids CHY and CUN with a variable resolution fully unstructured grid denoted by CUW.

5.2. Model validation and nonhydrostatic effects

The laminar curved channel flow is a good test case to demonstrate filter performance because noise in the horizontal divergence must be mitigated to resolve secondary flow features that arise from the nonlinear effective Coriolis term. A filter is not required provided nonhydrostatic pressure is computed and a hybrid grid is employed because high-frequency noise is relatively weak on this grid. To demonstrate model performance prior to filtering we compare the results of both hydrostatic and nonhydrostatic computations on hybrid grid CHY to the analytical results of deVriend (1981a) in Fig. 9. The transverse profile of primary streamwise flow $(u(\xi,\zeta=0))$ computed with the hydrostatic model in Fig. 9(a) is very noisy and, consequently, the vertical profile of primary streamwise flow $(u(\xi=0.5,\zeta))$ in Fig. 9(b) is skewed. The transverse profile of secondary vertical flow $(w(\xi,\zeta=-0.45))$ in Fig. 9(c) is composed of vertical velocities that are completely spurious for the hydrostatic case. The vertical profile of secondary transverse flow $(v(\xi=0.77,\zeta))$ in Fig. 9(d) is strongly damped for the hydrostatic flow as compared to the nonhydrostatic flow and the analytical solution. Filtering is generally necessary to resolve the correct vertical velocities because the secondary flow requires accurate computation of the dynamically important vertical velocities, particularly for hydrostatic flows. The primary flow $(u(\xi,\zeta))$ is also modified because noise from the horizontal divergence modes in Fig. 9(c) affects the horizontal velocity $(u(\xi,\zeta=0))$, as shown in Fig. 9(a). Consequently, unfiltered hydrostatic runs give rise to high-frequency oscillations in time which are not damped. As a

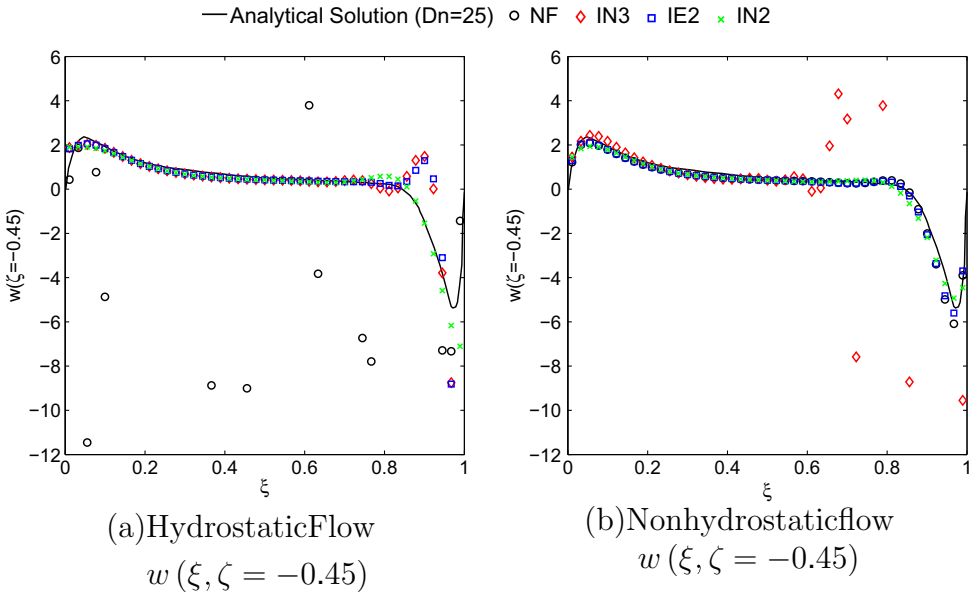

Fig. 11. Filter effects on secondary transverse horizontal flow structure for (a) hydrostatic and (b) nonhydrostatic flows. Comparison of non-filtered (NF – black ○), third-order implicit nodal filter (IN3 – red ◇), second-order implicit edge filter (IE2 – blue □), and second-order implicit nodal filter (IN2 – green ×) on grid FHY. The analytical solution for $Dn = 25$ (solid black line) is from deVriend (1981a). (For interpretation of the references to color in this figure legend, the reader is referred to the web version of this article.)

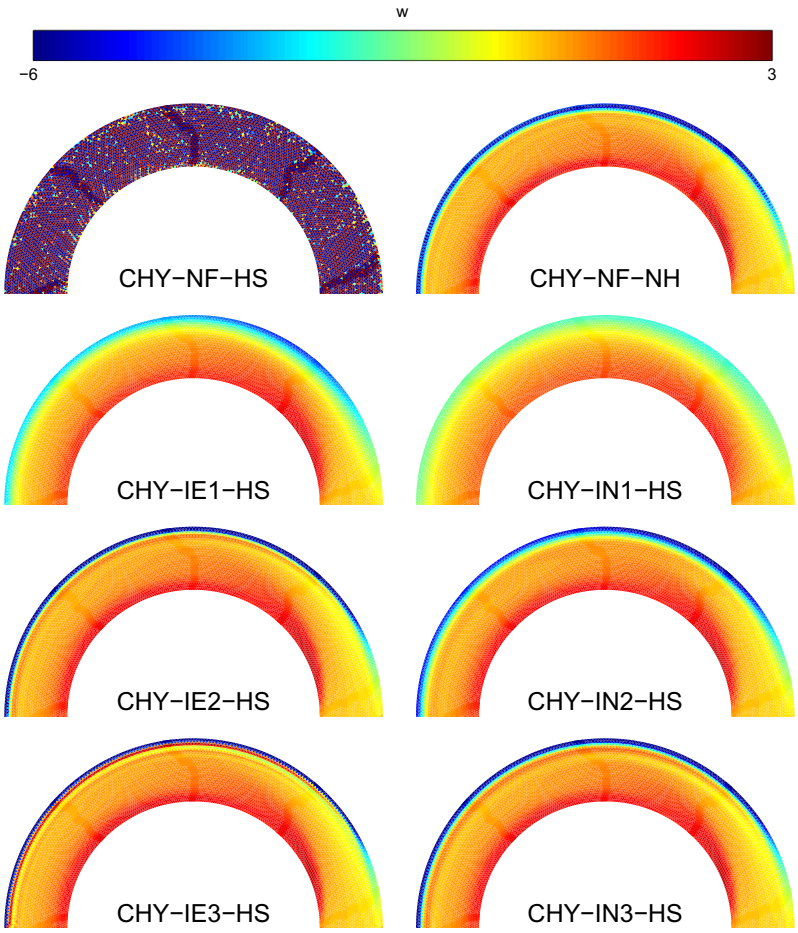

Fig. 12. Hydrostatic (HS) filtered vertical velocity fields $w(\phi, \xi, \zeta = -0.5)$ on grid CHY. The nonhydrostatic (NH) and the unfiltered (NF) solutions are given for comparison.

result, the unfiltered hydrostatic runs do not reach steady state for this laminar flow.

5.3. Filter accuracy on hybrid grids

In this section we assess the impacts of filtering on hybrid grid FHY for hydrostatic and nonhydrostatic flows. First-order through third-order implicit edge and nodal filters are utilized, where IE2 denotes a second-order edge filter and IN3 denotes a third-order nodal filter, etc. The root-mean-squared (RMS) errors associated with primary and secondary flow profiles for each filter applied to the hydrostatic and nonhydrostatic cases on hybrid grid FHY are given in Table A.2, Appendix A, as a reference. Fig. 10 highlights the RMS error for the transverse profile of secondary vertical flow, $w(\xi, \zeta = -0.45)$, which is most sensitive to filtering. The lowest errors for the primary flow are obtained with the second-order filters.

The most difficult flow to resolve is the secondary transverse flow $(w(\xi, \zeta = -0.45))$ because it is very sensitive to noise. Consequently, the degree to which filters can help simulate this flow determines their utility. For example, the IN2 filter performs better with respect to the hydrostatic flow for the secondary transverse flow $(w(\xi, \zeta = -0.45))$ as compared with the IE2 filter, with RMS error of 0.995 and 1.777, respectively. This is particularly evident in the secondary transverse flow profile because IN2 provides a drastically better fit for the hydrostatic flow as shown in Fig. 11(a). IE2 and IN3 performance is poor due to oscillations for both the hydrostatic and nonhydrostatic cases [Fig. 11(a)]. The IN2 filter provides the overall best fit and is a reasonable filter for practical use. However, for computations on hybrid grids with nonhydrostatic pressure, the IE2 filter is also a fine choice as shown in Fig. 11(b). Model results, particularly for the hydrostatic case, are improved with filtering because horizontal divergence errors are constrained. However, the quality and convergence of the final solution will vary depending upon the type of filter method used, grid quality and topology, and whether nonhydrostatic pressure is computed for weakly nonhydrostatic flows.

5.4. Spatial filter performance on fully unstructured grids

In this section we determine the spatial effects of filtering with respect to the type of unstructured grid employed for the hydrostatic and nonhydrostatic cases. Filter applicability for hydrostatic flows is evaluated by comparing the spatial performance of first-order, second-order, and third-order filters on fully unstructured grid CUN and hybrid grid CHY. Filter performance for nonhydrostatic flows is then assessed by comparing results for hybrid grid CHY and fully unstructured grids CUN (uniform resolution) and CUW (variable resolution) for second-order filters.

5.4.1. Spatial performance for hydrostatic flows

Filter performance varies depending on the grid type used. To illustrate this, we compare results obtained on coarse hybrid and uniform fully unstructured grids CHY and CUN, respectively, in hydrostatic runs. Fig. 12 compares the vertical velocity $(w(\phi, \xi, \zeta = -0.5))$ for grid CHY, showing that the filter methods IN2 perform best, as expected. The filter methods IN3, IE2, and IE3 result in an oscillatory vertical velocity, demonstrating the

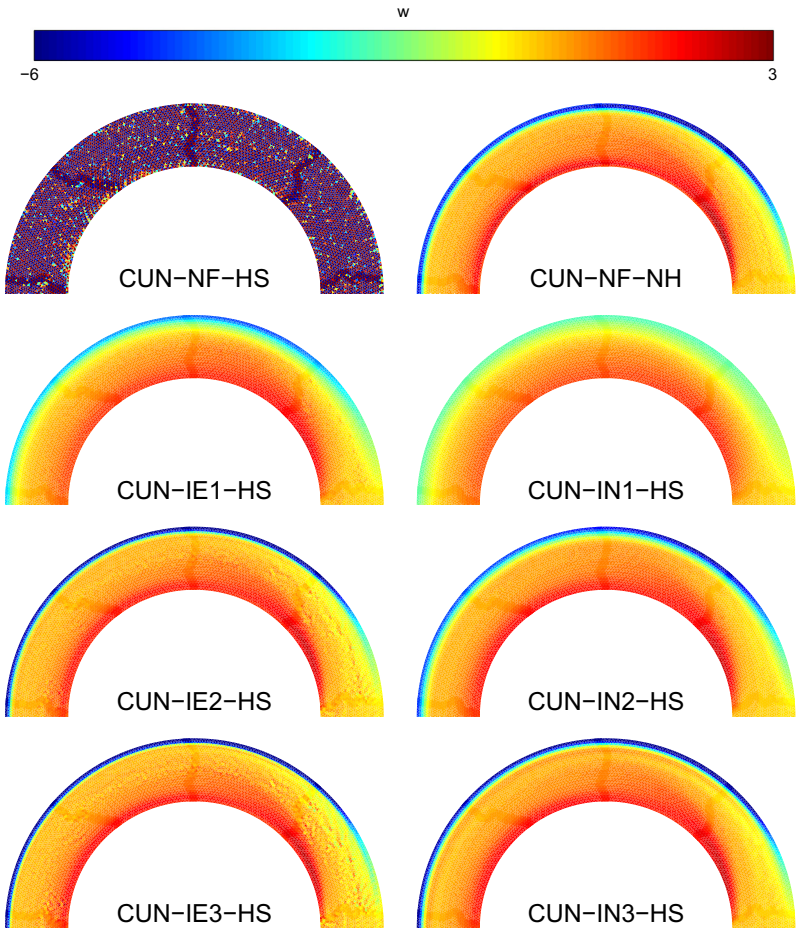

Fig. 13. Hydrostatic (HS) filtered vertical velocity fields $w(\phi, \xi, \zeta = -0.5)$ on grid CUN. The nonhydrostatic (NH) and the unfiltered (NF) solutions are given for comparison.

cause of their reduced accuracy as indicated by the RMS errors. The third-order filters IE3 and IN3 are oscillatory because of spurious dispersion induced by the filters.

Results are worse for the edge filters on a fully unstructured grid as shown in Fig. 13 because the edge filters cannot account for variations in grid topology. The IN2 filter is necessary to ensure that a variable grid topology containing five or seven cell neighbors at a node does not cause local solution irregularity. Nodal filters ensure smoothness of the horizontal divergence field by averaging these topological differences. The unfortunate cost, however, is reduced amplitude of the velocity signal. This is likely a necessary cost because the velocity is smooth on grid CHY and not on grid CUN for unfiltered nonhydrostatic simulations.

5.4.2. Spatial performance for nonhydrostatic flows

Nonhydrostatic pressure can help regulate the horizontal divergence in the absence of filtering in the case of a hybrid grid. However, in general, it cannot explicitly ensure that the horizontal divergence noise is removed. Implicit filtering is required to constrain the noise for a fully unstructured grid. An example is shown in Fig. 14 for $w(\phi, \xi, \zeta = -0.5)$, where grid variability for the unstructured grids is a source of the horizontal divergence noise. The hybrid grid does not require filtering to constrain the horizontal divergence noise because the nonhydrostatic pressure correction is sufficient to constrain the noise. The unstructured cases require filtering because nodes with other than six cell neighbors can be sources of noise accumulation and create local extrema in vertical velocity. Consequently, filtering is necessary to ensure locally smooth results. The nodal filters, in the absence of nonhydrostatic pressure, are alone sufficient to ensure a smooth solution on these grids. IN2 can sufficiently remove the horizontal divergence noise and assure a reasonable solution for the variable resolution fully unstructured grid CUW as shown in Fig. 14. The edge filter is insufficient to constrain the noise.

5.5. Temporal performance for fully unstructured grids

Spatial noise also manifests itself in time. Simulations utilizing the implicit edge filters IE1, IE2, and IE3 fail to converge to a smooth steady state on grid CUW. This is demonstrated with time series of the maximum horizontal Courant number $(\max(C_U))$ and maximum vertical Courant number $(\max(C_W))$ throughout the domain as shown in Fig. 15. Horizontal divergence noise results in temporal oscillation of the velocity field and consequently the maximum vertical Courant number corresponding to the secondary flow does not reach steady state. The IE2 filter produces a converged primary flow with an asymptotic maximum horizontal Courant number but the noise is insufficiently damped for the secondary flow, as noted by the oscillations of the maximum vertical Courant number. Only the IN2 case reaches steady state because errors in vertical velocities are constrained. The edge filter produces unsteadiness because, although much of the noise is eliminated, manifestation of noisy modes persists in time due to the spatially inconsistent topology of the fully unstructured grid. This is also evident by the noisy regions of vertical velocity shown in Fig. 14 for case CUW-IE2-NH. Consequently, only the nodal filter is sufficient to mitigate horizontal divergence noise in general.

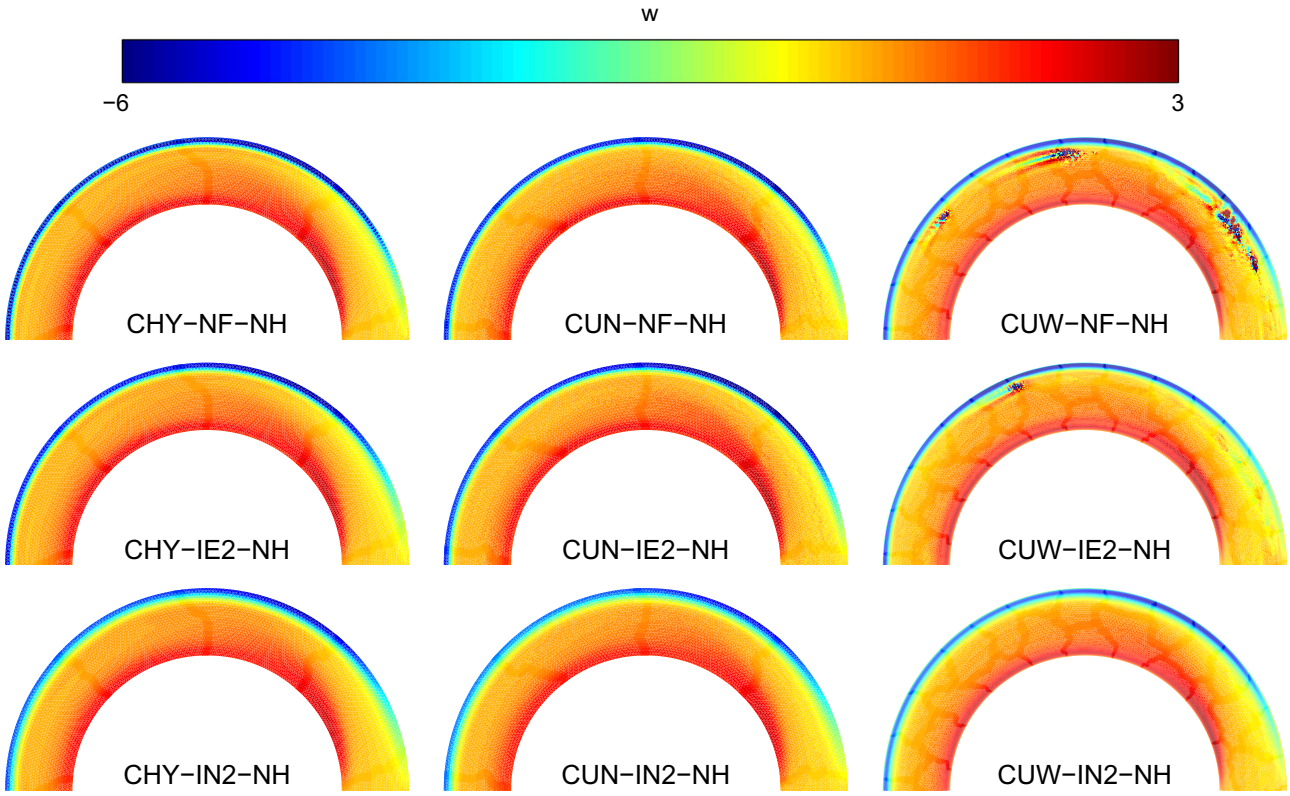

Fig. 14. Nonhydrostatic (NH) vertical velocity fields $w(\phi, \xi, \zeta = -0.5)$ for grids CHY, CUN, CUW. The unfiltered solutions (CHY-NF, CUN-NF, CUW-NF) are given for comparison with filter cases IE2 and IN2 for the hybrid (CHY-IE2, CHY-IN2), uniform resolution fully unstructured (CUN-IE2, CUN-IN2) and variable resolution fully unstructured grids (CUW-IE2, CUW-IN2).

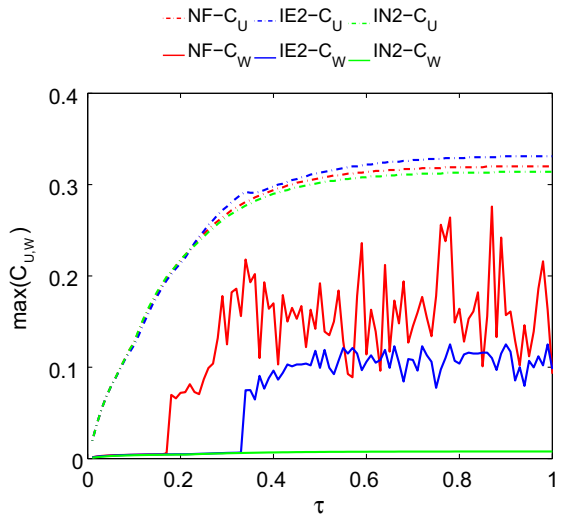

Fig. 15. Convergence in normalized time $\tau = t/t_{max}$ of solutions for variable resolution fully unstructured grid CUW. The maximum horizontal and maximum vertical Courant numbers [$\max(C_U)$ (dashed lines) and $\max(C_W)$ (solid lines), respectively] are plotted for the case of no filter (NF) in red, second-order edge filter (IE2) in blue, and second-order nodal filter (IN2) in green. Only the nodal filter results in a convergent solution. (For interpretation of the references to colour in this figure caption, the reader is referred to the web version of this article.)

6. Conclusions

We have shown that implicit filtering methods can mitigate horizontal divergence noise to allow calculation of secondary flows but at the cost of solving an elliptic corrector equation for each layer via a few relatively fast Gauss–Seidel iterations. Careful consideration of filter properties within the context of problem physics is warranted because these conclusions may change depending upon particular model configurations and flow regimes. However, general conclusions regarding practical use of filters to mitigate horizontal divergence error derived from this study are:

1. Implicit filtering provides the advantage of ensuring that the horizontal divergence is smooth, but its application requires solution of an elliptic equation with a high-frequency source term. The cost-differential between filter orders is minimal compared to the elliptic solution for the 3D corrector step. Use of the first-order explicit Perot filter (EP1), although appealing for its simplicity, is not recommended because it can increase the noise in the horizontal divergence field. The second-order explicit Perot filter (EP2) subsequently is not recommended. Development of suitable explicit filters is an open question and perhaps mimetic methods may provide the necessary framework.
2. The higher-order second- and third-order filters have less diffusion and thus do not directly modify the effective Reynolds number as the first-order filters do. The higher-order method performance is consequently less sensitive to the time step size. However, the third-order filter may be oscillatory suggesting that for most circumstances, a second-order filter is sufficient.
3. Filtering is in general necessary on a fully unstructured grid because nonhydrostatic pressure is insufficient to constraint the horizontal divergence noise. The second-order implicit edge filter (IE2) provides the sharpest results for a nonhydrostatic, hybrid grid case. However, these are restrictive conditions in practice. Nodal filters, in contrast, mitigate grid inhomogeneity, particularly in under-resolved regions. Consequently, the

Table A.1
Test case grid parameters. HY denotes a hybrid grid, UN denotes a uniform resolution fully unstructured grid, and UW denotes a variable resolution fully unstructured grid.

Grid name	Grid type	Total cells in 3D	$W/\Delta x$			$d/\Delta z$	$\frac{U_{max}\Delta t}{\Delta x_{min}}$
			mean	min	max		
FHY	HY	1,187,520	70.8	56.7	94.4	20	0.24
CHY	HY	187,650	40.5	32.1	53.1	10	0.34
CUN	UN	193,050	40.5	23.0	100	10	0.64
CUW	UW	528,260	73.9	25.0	340	10	0.54

Table A.2
Comparison of RMS error for primary and secondary flow profiles for filtered and unfiltered hydrostatic (HS) and nonhydrostatic (NH) flows. Filter abbreviations used: NF is no filter, IE1 is first-order implicit edge, IE2 is second-order implicit edge, IE3 is third-order implicit edge, IN1 is first-order implicit node, IN2 is second-order implicit node, IN3 is third-order implicit node.

p	Filter	RMS error			
		Primary flow		Secondary flow	
		Transverse $u(\xi, \zeta = 0)$	Vertical $u(\xi = 0.5, \zeta)$	Transverse $w(\xi, \zeta = -0.45)$	Vertical $v(\xi = 0.77, \zeta)$
HS	NF	0.265	0.192	41.91	6.762
	IE1	0.082	0.074	0.343	1.002
	IE2	0.042	0.062	1.777	1.721
	IE3	0.062	0.074	2.463	2.017
	IN1	0.112	0.069	0.385	2.577
	IN2	0.042	0.057	0.995	1.485
	IN3	0.040	0.061	1.720	1.719
NH	NF	0.058	0.056	0.803	1.146
	IE1	0.082	0.062	0.269	1.036
	IE2	0.059	0.054	0.721	1.009
	IE3	0.059	0.055	0.764	1.047
	IN1	0.114	0.065	0.380	2.591
	IN2	0.056	0.055	0.654	1.263
	IN3	0.389	0.206	12.84	18.07

second-order implicit nodal filter (IN2) provides the best performance for hydrostatic and arbitrary, multi-scale unstructured triangular C-grid cases and it is likely the best choice in practice.

The novel filters presented in this paper improve the viability of unstructured triangular C-grids for nonlinear and nonhydrostatic flows. The primary cost of the implicit filtering methods is the elliptic inversion of the filtering Poisson equation (9). Perhaps clever design of an explicit filter without the pitfalls of the Perot filters may provide filtering without requiring smoothing via an iterative solution to Eq. (9). This remains an open question. However, for problems with strong nonlinearity and important secondary flows, the implicit elliptic filtering methods developed in this paper are sufficient to mitigate the horizontal divergence noise and eliminate contamination of the solution via nonlinear feedback. Further work is also needed to address the problem of filtering in the presence of variable topography.

Acknowledgements

P.J. Wolfram gratefully acknowledges the support of the Office of Naval Research (ONR) through the National Defense Science & Engineering Graduate Fellowship (NDSEG) Program, computer time at the at Army Research Lab DSRC (ONRDC27755267), and additional funding through the Delta Science program. P.J. Wolfram and O.B. Fringer gratefully acknowledge the support of ONR Grant N00014-10-1-0521 as part of the PECASE award (scientific officers Dr. C. Linwood Vincent, Dr. Terri Paluszkiewicz and Dr. Scott Harper). We are indebted to Sergey Danilov and two anonymous reviewers for their insightful and helpful comments which greatly improved the quality of this manuscript. Conversations with Todd Ringler, Sergey Danilov, Derek Fong, Bing Wang, Rusty Holleman, Ed Gross, Michael MacWilliams, and Sean Vitousek were particularly helpful during development and refinement of these ideas.

Appendix A. Model parameters and RMS errors

See Tables A.1 and A.2.

References

Adcroft, A., Hill, C., Campin, J., Marshall, J., Heimbach, P., 2004. Overview of the formulation and numerics of the mit gcm. In: Proceedings of the ECMWF Seminar Series on Numerical Methods, Recent Developments in Numerical Methods for Atmosphere and, Ocean Modelling, pp. 139–149.

Aris, R., 1956. On the dispersion of a solute in a fluid flowing through a tube. Proceedings of the Royal Society of London. Series A. Mathematical and Physical Sciences 235, 67–77.

Berntsen, J., Xing, J., Alendal, G., 2006. Assessment of non-hydrostatic ocean models using laboratory scale problems. Continental Shelf Research 26, 1433–1447.

Casulli, V., Zanolli, P., 2002. Semi-implicit numerical modeling of nonhydrostatic free-surface flows for environmental problems. Mathematical and Computer Modelling 36, 1131–1149.

Casulli, V., Zanolli, P., 2005. High resolution methods for multidimensional advection–diffusion problems in free-surface hydrodynamics. Ocean Modelling 10, 137–151.

Danilov, S., 2010. On utility of triangular C-grid type discretization for numerical modeling of large-scale ocean flows. Ocean Dynamics 60, 1361–1369.

deVriend, H., 1981a. Steady flow in shallow channel bends. Ph.D. thesis, T.U. Delft.

deVriend, H., 1981b. Velocity redistribution in curved rectangular channels. Journal of Fluid Mechanics 107, 423–439.

Fringer, O., Gerritsen, M., Street, R., 2006. An unstructured-grid, finite-volume, nonhydrostatic, parallel coastal ocean simulator. Ocean Modelling 14, 139–173.

Gassmann, A., 2011. Inspection of hexagonal and triangular C-grid discretizations of the shallow water equations. Journal of Computational Physics 230, 2706–2721.

Holleman, R., Fringer, O., Stacey, M., 2013. Numerical diffusion for flow-aligned unstructured grids with application to estuarine modeling. International Journal for Numerical Methods in Fluids, http://dx.doi.org/10.1002/fld.3774.

Huebner, K., 1975. The Finite Element Method for Engineers. John Wiley and Sons.

Jankowski, J., 2009. Parallel implementation of a non-hydrostatic model for free surface flows with semi-lagrangian advection treatment. International Journal for Numerical Methods in Fluids 59, 1157–1179.

Klinger, B., Cruz, C., Schopf, P., 2006. Targeted shapiro filter in an ocean model. Ocean Modelling 13, 148–155.

Korn, P., 2011. On ICON and its mimetic ocean, Presentation at Los Alomos National Laboratory, Santa Fe, NM, August 4, 2011.

Le Roux, D., Rostand, V., Pouliot, B., 2007. Analysis of numerically induced oscillations in 2d finite-element shallow-water models part i: inertia-gravity waves. SIAM Journal on Scientific Computing 29, 331–360.

Nicolaides, R., 1992. Direct discretization of planar div–curl problems. SIAM Journal on Numerical Analysis 29, 32–56.

Perot, B., 2000. Conservation properties of unstructured staggered mesh schemes. Journal of Computational Physics 159, 58–89.

Ringler, T., Petersen, M., Jacobsen, D., Maltrud, M., Jones, P., 2013. A multi-resolution approach to global ocean modeling. Ocean Modelling, http://dx.doi.org/10.1016/j.ocemod.2013.04.010.

Rípodas, P., Gassmann, A., Förstner, J., Majewski, D., Giorgetta, M., Korn, P., Kornblueh, L., Wan, H., Zängl, G., Bonaventura, L., Heinze, T., 2009. Icosahedral shallow water model (ICOSWM): results of shallow water test cases and sensitivity to model parameters. Geoscientific Model Development 2, 231–251.

Shapiro, R., 1975. Linear filtering. Mathematics of Computation 29, 1094–1097.

Shchepetkin, A., McWilliams, J., 2005. The regional oceanic modeling system (ROMS): a split-explicit, free-surface, topography-following-coordinate oceanic model. Ocean Modelling 9, 347–404.

Shuman, F., 1957. Numerical methods in weather prediction: II. Smoothing and filtering. Monthly Weather Review 85, 357–361.

Vitousek, S., Fringer, O.B., 2012. Stability and consistency of nonhydrostatic free-surface models using the semi-implicit h-method. International Journal for Numerical Methods in Fluids 72, 550–582.

Walters, R., Hanert, E., Pietrzak, J., Le Roux, D., 2009. Comparison of unstructured, staggered grid methods for the shallow water equations. Ocean Modelling 28, 106–117.

Wan, H., Giorgetta, M.A., Zängl, G., Restelli, M., Majewski, D., Bonaventura, L., Fröhlich, K., Reinert, D., Rípodas, P., Kornblueh, L., 2013. The icon-1.2 hydrostatic atmospheric dynamical core on triangular grids part 1: formulation and performance of the baseline version. Geoscientific Model Development Discussions 6, 59–119.

Wang, B., Zhao, G., Fringer, O., 2011. Reconstruction of vector fields for semi-lagrangian advection on unstructured, staggered grids. Ocean Modelling 40, 52–71.